



Calculation and Uncertainty of Fast Radio Burst Structure Based on Smoothed Data

Adrian T. Sutinjo¹, Danica R. Scott¹, Clancy W. James¹, Marcin Glowacki¹, Keith W. Bannister², Hyerin Cho (조혜린)^{3,4}, Cherie K. Day⁵, Adam T. Deller⁵, Timothy P. Perrett¹, and Ryan M. Shannon⁵

¹International Centre for Radio Astronomy Research, Curtin University, Bentley, WA 6102, Australia

²ATNF, CSIRO, Space and Astronomy, PO Box 76, Epping, NSW 1710, Australia

³Center for Astrophysics | Harvard & Smithsonian, 60 Garden Street, Cambridge, MA 02138, USA

⁴Black Hole Initiative at Harvard University, 20 Garden Street, Cambridge, MA 02138, USA

⁵Centre for Astrophysics and Supercomputing, Swinburne University of Technology, Hawthorn, VIC 3122, Australia

Received 2023 February 13; revised 2023 July 9; accepted 2023 July 12; published 2023 August 31

Abstract

Studies of the time-domain structure of fast radio bursts (FRBs) require an accurate estimate of the FRB dispersion measure in order to recover the intrinsic burst shape. Furthermore, the exact dispersion measure is itself of interest when studying the time evolution of the medium through which multiple bursts from repeating FRBs propagate. A commonly used approach to obtain the dispersion measure is to take the value that maximizes the FRB structure in the time domain. However, various authors use differing methods to obtain this structure parameter and do not document the smoothing method used. Furthermore, there are no quantitative estimates of the error in this procedure in the FRB literature. In this article, we present a smoothing filter based on the discrete cosine transform, and show that computing the structure parameter by summing the squares of the derivatives and taking the square root (that is, the 2-norm, $\sqrt{\Sigma(d/dt)^2}$) immediately lends itself to the calculation of the uncertainty of the structure parameter. We illustrate this with FRB 20181112A and FRB 20210117A data, which were detected by the Australian Square Kilometre Array Pathfinder, and for which high-time-resolution data are available.

Unified Astronomy Thesaurus concepts: [Radio transient sources \(2008\)](#)

1. Introduction

Fast radio bursts (FRBs) are extragalactic radio transients of millisecond duration (Lorimer et al. 2007). Both the underlying mechanism of their emission, and the properties of the astrophysical plasmas through which they propagate, can be studied through detailed analysis of their time-frequency structure (e.g., Michilli et al. 2018; Macquart et al. 2020). The frequency-dependent delay (dispersion measure (DM)) of FRBs informs about the total integrated column density of free electrons—and hence total matter density—through which the FRB has propagated. Long-term studies of DM variation in repeating FRBs yield information on the medium in the vicinity of the progenitor (e.g., Zhao et al. 2021). Additionally, studies of FRB structure are sensitive to the assumed value of DM used to dedisperse the FRB (e.g., Hessels et al. 2019). To this end, FRB analysis aims to identify the correct DM, i.e., that corresponds to the integrated electron column density through which the FRB has passed. While FRB searches use the dispersion measure that maximizes the signal-to-noise ratio (S/N), it is often assumed that the correct DM is that which maximizes structure (Caleb et al. 2020; Hilmarsson et al. 2021; Platts et al. 2021).

A common measure of structure is the time-derivative of the pulse intensity $I(t)$ (Gajjar et al. 2018; CHIME/FRB Collaboration, et al. 2019; Hessels et al. 2019; Josephy et al. 2019; Pilia et al. 2020). However, since $I(t)$ is noisy, the derivative operation is not applied to a noisy estimate of the $I(t)$, but rather to a smoothed version thereof. This smoothing

operation has the potential to affect the structure-maximizing DM, since oversmoothing will smear out the intrinsic FRB structure, while undersmoothing will leave the derivative dominated by noise. However, to date, there has been little attention paid to how to optimally select a smoothing time.

In the literature, there is also a slight variation in how the resulting d/dt are combined. For example, Hessels et al. (2019) used $\Sigma(d/dt)^2$, Gajjar et al. (2018) suggested $\Sigma|d/dt|$, and Josephy et al. (2019) experimented with $\Sigma(d/dt)^4$. One may argue that this is a matter of preference as long as the positive of the d/dt is combined and an interesting structure is detected. However, while any of these approaches should be able to identify the DM that maximizes the structure in the signal, the uncertainty of the resultant fitted DM is also of considerable interest—without an accurate estimate of this uncertainty, it is impossible to determine whether, for instance, the DM of a given source is changing between bursts.

In Section 2, we shall demonstrate that the vector norm offers a meaningful measure of the uncertainty in the structure parameter inferred from noisy time-series data. In particular, the $\sqrt{\Sigma(d/dt)^2}$ (Euclidean or 2-norm) offers a physical and intuitive interpretation, as illustrated in Section 3. Section 4 then illustrates how the structure parameter, and uncertainty thereon, are to be calculated for two example FRBs. Under the assumption that the “correct” DM of an FRB⁶ is synonymous with structure maximization, this allows the correct DM to be identified and assigned an uncertainty $\pm\Delta\text{DM}$, which quantifies the confidence in such a detection.

Original content from this work may be used under the terms of the [Creative Commons Attribution 4.0 licence](#). Any further distribution of this work must maintain attribution to the author(s) and the title of the work, journal citation and DOI.

⁶ i.e., such that $\text{DM} = \int n(e)(1+z)^{-1} dl$ for electron density $n(e)$ and unique signal propagation path dl .

2. Method

2.1. Matrix Representation and Uncertainty Definition

Let $\mathbf{i} = [I(1), \dots, I(N)]^T$ be a vector that contains discrete time samples of noisy total intensity $I(t)$. We may represent the smoothing operator as a matrix \mathbf{S} and the first derivative as a matrix \mathbf{D}_1 . Our immediate discussion here pertains to any \mathbf{S} and \mathbf{D}_1 matrices; therefore, the conclusions are generally applicable. It suffices to say, as we shall demonstrate later, that it is indeed possible to write the smoothing algorithm as a matrix; for example, see Strang & Nguyen (1997), Eilers (2003), and Stickel (2010). The result of the smoothing process is the smoothed estimate

$$\tilde{\mathbf{i}} = \mathbf{S}\mathbf{i}. \quad (1)$$

The first derivative operator can be expressed as a matrix, for example, a simple forward difference on N data points is a $(N-1) \times N$ matrix

$$\mathbf{D}_1 = \begin{bmatrix} -1 & 1 & & & \\ & & \ddots & & \\ & & & \ddots & \\ & & & & -1 & 1 \end{bmatrix}. \quad (2)$$

Therefore, the first derivative of the smoothed data is

$$\mathbf{D}_1\tilde{\mathbf{i}} = \mathbf{D}_1\mathbf{S}\mathbf{i}. \quad (3)$$

The original noisy data can be expressed as the sum of the smoothed estimate and the difference between the noisy data and the smoothed version $\Delta_i = \mathbf{i} - \tilde{\mathbf{i}}$.

$$\mathbf{i} = \tilde{\mathbf{i}} + \Delta_i. \quad (4)$$

Therefore, Equation (3) may be written as

$$\begin{aligned} \mathbf{D}_1\tilde{\mathbf{i}} &= \mathbf{D}_1\mathbf{S}(\tilde{\mathbf{i}} + \Delta_i) \\ &= \mathbf{D}_1\mathbf{S}\tilde{\mathbf{i}} + \mathbf{D}_1\mathbf{S}\Delta_i. \end{aligned} \quad (5)$$

Equation (5) is illustrated in Figure 1. We note that the first term on the right-hand side of Equation (5), $\mathbf{D}_1\mathbf{S}\tilde{\mathbf{i}} = \mathbf{D}_1\mathbf{S}\mathbf{S}\mathbf{i}$, is the derivative of the ‘‘double-smoothed’’ data. The second term, $\mathbf{D}_1\mathbf{S}\Delta_i$, is the derivative of the smoothed ‘‘detrended’’ noise.

The length (2-norm, $\|\cdot\|_2$) of $\mathbf{D}_1\mathbf{S}\Delta_i$ is the radius of the dashed circle in Figure 1, which may be written as

$$\|\mathbf{D}_1\mathbf{S}\Delta_i\|_2 = \sqrt{\sum_{n=1}^N [(D_1\mathbf{S}\mathbf{i})_n - (D_1\mathbf{S}\tilde{\mathbf{i}})_n]^2}, \quad (6)$$

where $(\cdot)_n$ indicates the n -th element of the vector in question. The right-hand side of Equation (6) suggests that it can be interpreted as proportional to a standard deviation estimate ($\tilde{\sigma}\sqrt{N-1}$) of the first derivative of the smoothed data. Taking this as the uncertainty estimate of $\mathbf{D}_1\tilde{\mathbf{i}}$ means we take $\mathbf{D}_1\mathbf{S}\Delta_i$ to represent a particular noise instance with standard deviation of $\|\mathbf{D}_1\mathbf{S}\Delta_i\|_2/\sqrt{N-1}$. In that case, the tip of the vector $\mathbf{D}_1\tilde{\mathbf{i}}$ in Figure 1 could lie anywhere on the circumference of the gray circle, such that the estimate of relative uncertainty may be computed as

$$\frac{\|\mathbf{D}_1\mathbf{S}\Delta_i\|_2}{\|\mathbf{D}_1\mathbf{S}\tilde{\mathbf{i}}\|_2}. \quad (7)$$

The structure parameter that is consistent with this uncertainty estimate is, evidently, the 2-norm of the $\mathbf{D}_1\tilde{\mathbf{i}}$ since

$$\|\mathbf{D}_1\mathbf{S}\tilde{\mathbf{i}}\| - \|\mathbf{D}_1\mathbf{S}\Delta_i\| \leq \|\mathbf{D}_1\tilde{\mathbf{i}}\| \leq \|\mathbf{D}_1\mathbf{S}\tilde{\mathbf{i}}\| + \|\mathbf{D}_1\mathbf{S}\Delta_i\|, \quad (8)$$

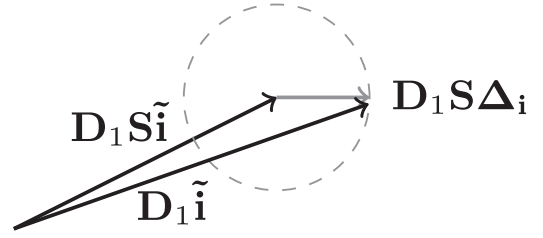


Figure 1. Vector diagram representing Equation (5).

where the subscript $_2$ is not shown (and hereafter) for brevity. Equation (8) is valid for the 2-norm for N -dimensional vectors. It can be shown formally by applying the inner product definition $\mathbf{x}^T\mathbf{y} = \|\mathbf{x}\|\|\mathbf{y}\|\cos\theta$ in the expression $\|\mathbf{x} + \mathbf{y}\|^2 = (\mathbf{x} + \mathbf{y})^T(\mathbf{x} + \mathbf{y})$ (see Ch. 1 of Strang 2019) and realizing that $-1 \leq \cos\theta \leq 1$ for real vectors.

In reality, the data are vectors with N entries. In that case, the circumference of the circle in Figure 1 becomes the surface of an N -dimensional sphere with the same radius. The conclusion is unchanged.

For some applications, it may be desirable to test the hypothesis of whether the intrinsic structure in a signal \mathbf{i}_1 is significantly greater than that in another signal \mathbf{i}_2 . This test asks whether or not the measured difference in structure

$$\|\mathbf{D}_1\mathbf{S}\mathbf{i}_1\| - \|\mathbf{D}_1\mathbf{S}\mathbf{i}_2\| \quad (9)$$

is significant compared to the relative noise,

$$\|\mathbf{D}_1\mathbf{S}\Delta_{i_1} - \mathbf{D}_1\mathbf{S}\Delta_{i_2}\| = \|\mathbf{D}_1\mathbf{S}(\Delta_{i_1} - \Delta_{i_2})\|. \quad (10)$$

Continuing the analogy of Figure 1, Equation (10) represents the surface of an n -dimensional sphere with magnitude given by a combination of $\mathbf{D}_1\mathbf{S}\Delta_{i_1}$ and $\mathbf{D}_1\mathbf{S}\Delta_{i_2}$. If the difference in structure between \mathbf{i}_1 and \mathbf{i}_2 given by Equation (9) is less than the radius of the sphere, the structures are consistent to within noise fluctuations. Specifically, the structure in \mathbf{i}_1 can be said to be greater than that in \mathbf{i}_2 when

$$\|\mathbf{D}_1\mathbf{S}\mathbf{i}_1\| > \|\mathbf{D}_1\mathbf{S}\mathbf{i}_2\| + \|\mathbf{D}_1\mathbf{S}(\Delta_{i_1} - \Delta_{i_2})\|. \quad (11)$$

Such a test will become relevant when assessing whether the structure at one DM is significantly different from the structure at another, since Δ_{i_1} and Δ_{i_2} will in this case be correlated.

2.2. Example Smoothing Matrix Based on Discrete Cosine

We can choose the eigenvectors of $\mathbf{D}_1^T\mathbf{D}_1$ as the basis for the smoothing operation. As we will show later, the close connection to the first derivative \mathbf{D}_1 matrix lends itself to insight when expressing the entire calculation as a single matrix operation. The eigenvectors of

$$\mathbf{D}_1^T\mathbf{D}_1 = \begin{bmatrix} -1 & 1 & & & \\ -1 & 2 & -1 & & \\ & \cdot & \cdot & \cdot & \\ & & -1 & 2 & -1 \\ & & & -1 & 1 \end{bmatrix}, \quad (12)$$

are discrete cosines (Strang 1999). We shall call this eigenvector matrix \mathbf{C} whose components are

$$c_k(j) = \cos\left(j - \frac{1}{2}\right)\frac{(k-1)\pi}{N}, \quad (13)$$

where $k = 1, \dots, N$ is the column number of \mathbf{C} and $j = 1, \dots, N$ is the row number. The eigenvalues are

$$\text{eig}_k = 2 - 2 \cos \frac{(k-1)\pi}{N}. \quad (14)$$

This is known as the discrete cosine transform-2 (DCT-2). Most importantly, DCT-2 has a fast implementation based on the fast Fourier transform (FFT; Strang 1999). Therefore, numerical linear algebra eigendecomposition is not needed to obtain Equations (13) and (14).

The smoothing operation may be written as

$$\tilde{\mathbf{i}} = \mathbf{C} \mathbf{D}_{\text{filter}} \mathbf{C}^T \mathbf{i} = \mathbf{S} \mathbf{i}, \quad (15)$$

where $\mathbf{D}_{\text{filter}}$ is a diagonal matrix representing a low-pass filter in the spectral domain; $\mathbf{C}^T \mathbf{i}$ is the DCT of \mathbf{i} and $\mathbf{C}(\mathbf{D}_{\text{filter}} \mathbf{C}^T \mathbf{i})$ is the inverse DCT of the filtered spectrum. The diagonal of $\mathbf{D}_{\text{filter}}$ is the spectral response of a low-pass filter, for example,

$$f(k) = \frac{1}{1 + \left(\frac{k}{k_c}\right)^{2O}}, \quad (16)$$

where k_c is the spectral cutoff and O is the order of the filter. The resulting passband is flat and the roll-off rate is $2O$ orders of magnitude per decade, as inspired by the analog Butterworth filter. The DCT is purely real and does not force a periodic boundary condition (as in the case of FFT) that could introduce a discontinuity corresponding to high-frequency contents (Strang & Nguyen 1997, see Ch. 8).

Using the smoothing process based on the DCT in Equation (15), we can write

$$\begin{aligned} \|\mathbf{D}_1 \tilde{\mathbf{i}}\|^2 &= \mathbf{i}^T \mathbf{C} \mathbf{D}_{\text{filter}} \mathbf{C}^T \mathbf{D}_1^T \mathbf{D}_1 \mathbf{C} \mathbf{D}_{\text{filter}} \mathbf{C}^T \mathbf{i} \\ &= \mathbf{i}^T \mathbf{C} \mathbf{D}_{\text{filter}} \mathbf{\Lambda}_{\mathbf{D}_1^T \mathbf{D}_1} \mathbf{D}_{\text{filter}} \mathbf{C}^T \mathbf{i} \\ &= \|\mathbf{\Lambda}_{\mathbf{D}_1^T \mathbf{D}_1}^{1/2} \mathbf{D}_{\text{filter}} \mathbf{C}^T \mathbf{i}\|^2 \end{aligned} \quad (17)$$

where we used the eigendecomposition $\mathbf{D}_1^T \mathbf{D}_1 = \mathbf{C} \mathbf{\Lambda}_{\mathbf{D}_1^T \mathbf{D}_1} \mathbf{C}^T$ and $\mathbf{\Lambda}_{\mathbf{D}_1^T \mathbf{D}_1}$ is a diagonal matrix of nonnegative eigenvalues, eig_k , shown in Equation (14); $\mathbf{C}^T \mathbf{C} = \mathbf{I}$ since \mathbf{C} is an orthogonal matrix. Equation (17) is a key result. It expresses the final product, which is the sum of the square of the derivative of the smoothed data in terms of the end-to-end matrix operation. We note that $\mathbf{\Lambda}_{\mathbf{D}_1^T \mathbf{D}_1}^{1/2}$ is a diagonal matrix whose diagonal represents a high pass profile such that $\mathbf{\Lambda}_{\mathbf{D}_1^T \mathbf{D}_1}^{1/2} \mathbf{D}_{\text{filter}}$ represents a bandpass filter with the peak response at approximately k_c , as shown in Figure 2. The norm of the smoothed data is the structure parameter, $\sqrt{\Sigma(d/dt)^2}$,

$$\|\mathbf{D}_1 \tilde{\mathbf{i}}\| = \|\mathbf{\Lambda}_{\mathbf{D}_1^T \mathbf{D}_1}^{1/2} \mathbf{D}_{\text{filter}} \mathbf{C}^T (\tilde{\mathbf{i}} + \mathbf{\Delta}_i)\|. \quad (18)$$

Finally, the uncertainty is

$$\|\mathbf{D}_1 \mathbf{S} \mathbf{\Delta}_i\| = \|\mathbf{\Lambda}_{\mathbf{D}_1^T \mathbf{D}_1}^{1/2} \mathbf{D}_{\text{filter}} \mathbf{C}^T \mathbf{\Delta}_i\|. \quad (19)$$

Expressing the 2-norm in the spectral domain as we have done above has an advantage in visualization. For example, $\mathbf{C}^T \mathbf{i}$ is the spectrum of $I(t)$. Premultiplying that quantity by $\mathbf{\Lambda}_{\mathbf{D}_1^T \mathbf{D}_1}^{1/2} \mathbf{D}_{\text{filter}}$ filters the spectrum. Finally, taking the norm measures the length of the resulting vector.

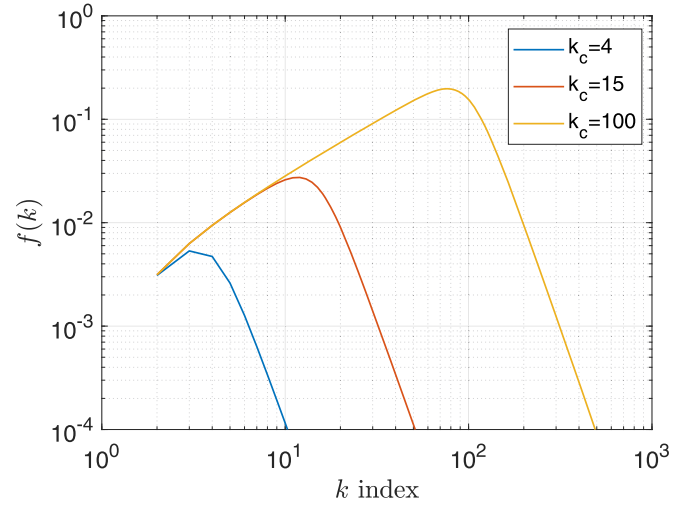


Figure 2. $\mathbf{\Lambda}_{\mathbf{D}_1^T \mathbf{D}_1}^{1/2} \mathbf{D}_{\text{filter}}$ bandpass filter response for $k_c = 4, 15,$ and 100 for an $O = 3$ filter defined by Equation (16).

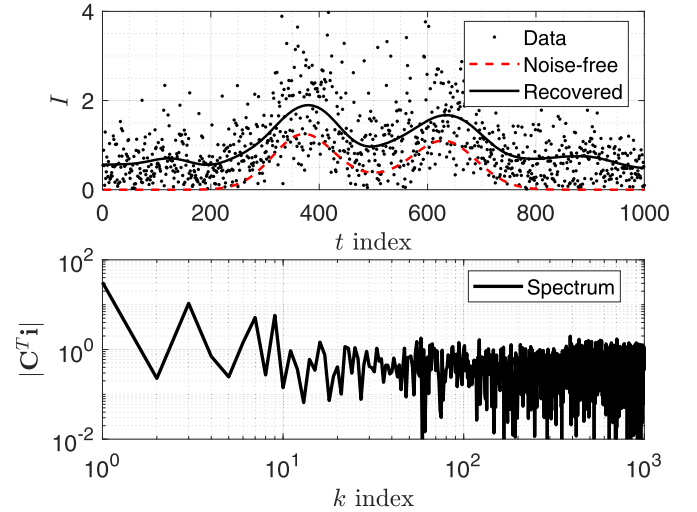


Figure 3. Example noisy pulse (top) and the corresponding spectrum in discrete cosine (bottom). The underlying pulse consists of two unity amplitude Gaussians shown as the red dashed line in the top panel. The offset seen in the black curve is due to additive noise in the simulated noisy data. The solid black curve in the top plot represents the recovered intensity with filter parameters $O = 3$ and $k_c = 15$.

3. Result: Numerical Example

3.1. Selection of Filter Parameters

We exemplify the method discussed in Section 2.2 by demonstrating the selection of filter parameters to correctly recover the underlying $I(t)$ structure in the presence of noise. Figure 3 (top) shows 1000 noisy $I = |X|^2 + |Y|^2$ data points with an underlying double pulse as shown, representing total power I calculated from perpendicular X and Y linearly polarized voltage components. The noise-free component of X consists of two Gaussian pulses delayed by 370 and 630 units with standard deviations of 80 and 85, respectively. The amplitude is normalized to the pulse peak. The noise-free amplitude of the Y component is taken as $0.5X$. The structure parameter of the noise-free pulse is $\|\mathbf{D}_1 \mathbf{i}_{\text{noiseless}}\| = 0.18$ as computed by the 2-norm of the first derivative. The noise in the complex voltages X and Y are independent and identically

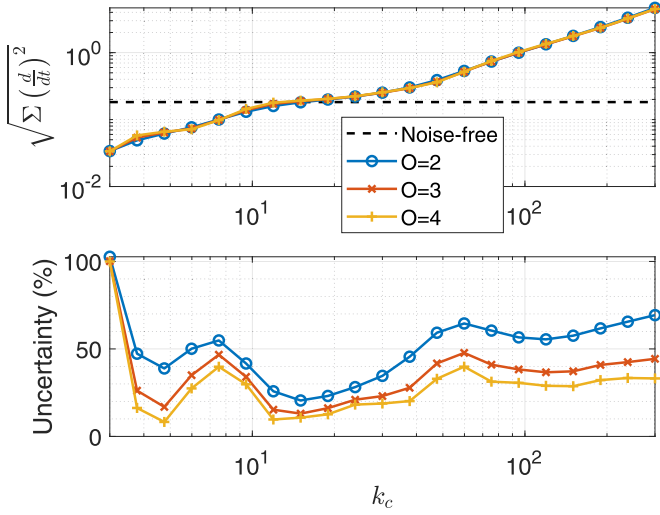


Figure 4. Recovered structure parameter (top) and uncertainty (bottom) of the structure parameter for k_c swept from 3 to 300 and filter order 2, 3, and 4 in Equation (16).

distributed Gaussian noise with zero mean and standard deviation $\sigma_{\Re(X)} = \sigma_{\Im(X)} = \sigma_{\Re(Y)} = \sigma_{\Im(Y)} = 0.4$. The DCT spectrum of the signal is depicted in Figure 3 (bottom). It shows that the information occupies up to a k index of 10 to 20, beyond which the noise dominates. Therefore, we expect to select a low-pass filter cutoff between k_c of 10 to 20.

The k_c estimate based on the DCT spectrum is confirmed by the calculated structure parameter and the uncertainty shown in Figure 4 where the low-pass filter cutoff k_c was swept from 3 to 300 for filter order 2, 3, and 4 in Equation (16) to explore the effects of under- and overfiltering. The structure parameter was computed using Equation (18) and the associated uncertainty was calculated using Equation (7). The structure parameter obtained from the smoothed noisy data matches the known noise-free value of 0.18 for k_c between 10 to 20, which agrees with that suggested by the DCT spectrum. This also coincides with the range of k_c values for which the uncertainty is minimized. We also note that the structure parameter becomes rapidly underestimated and overestimated as the k_c is underestimated (oversmoothing) and overestimated (undersmoothing), respectively. The uncertainty minima at k_c of approximately 5 for filter orders 3 and 4 in Figure 4 correspond to oversmoothing, which may be readily identified from the DCT spectrum in Figure 3 and confirmed by the recovered structure parameter. Proper determination of k_c is therefore critical, and we demonstrate that the DCT spectrum is a very effective tool for that purpose.

3.2. Robustness with Respect to ΔDM

The previous subsection operated on one-dimensional time-series data, which assumes that dedispersion has already been performed. However, in reality, the dispersion measure is not known a priori (otherwise the problem would already be solved), and hence it is necessary to consider whether dedispersing across different trial DM values could affect the parameter choice and hence final results. In this subsection, we simulate the effects of dispersion and dedispersion on the double pulse already considered.

In the frequency domain, the net effect of dispersion and dedispersion may be described as a multiplicative factor

$$e^{-j(k(\nu) - \tilde{k}(\nu))L} = e^{-j(2\pi)K_{DM} \frac{-\Delta DM [\text{pc cm}^{-3}]}{\nu [\text{MHz}]}}. \quad (20)$$

The units in Equation (20) follow the convention described in Wilson et al. (2009); L is the distance to the source and $k(\nu)$ and $\tilde{k}(\nu)$ are the wavenumber and the wavenumber estimate, respectively; the difference between the actual DM and the DM estimate is $\Delta DM = DM - \tilde{DM}$. Throughout, we define the delay constant K_{DM} to be $(1/0.241) \times 10^9 \approx 4.149 \times 10^9 \text{ MHz cm}^3 \text{ pc}^{-1}$. Hence, the effects of dispersion and dedispersion may be simulated by multiplying Equation (20) with the Fourier transform (FT) of the noisy complex voltages, followed by the inverse FT of the product.

As an example, we took a 256×1024 matrix of complex white noise with $\sigma_{re} = \sigma_{im} = 1/\sqrt{2}$. This noise matrix was multiplied by two two-dimensional Gaussian real envelopes, and then complex Gaussian noise with $\sigma_{re} = \sigma_{im} = 1/2\sqrt{2}$ was added. The results shown in the top and middle left panels in Figure 5 represent the simulated data at $\Delta DM = 0$. We chose the time delays between the components to mimic the ‘‘sad trombone’’ effect, i.e., the frequency down-drift of burst components with time, often seen in repeating FRBs (e.g., Hessels et al. 2019).

We applied ΔDM from -0.5 to 0.2 pc cm^{-3} in 0.01 pc cm^{-3} steps. The resulting noisy mean intensities versus time over ΔDM are shown in the bottom left panel of Figure 5. The intensity of the noise-free data was simulated by applying the corresponding group delay $\tau_d = 4.149 \times 10^3 \Delta DM [\text{pc cm}^{-3}] / f_{\text{MHz}}^2$ to the intensity envelope. To filter the noise, we applied the same strategy discussed in Section 3.1. We performed DCT of the frequency-time 256×1024 data shown and then visually inspected the resulting DCT spectrum shown in the top right panel of Figure 5. The transition between information and noise occurred at a k index of approximately 35. Therefore, we set $k_c = 35$, and $O = 3$ was kept the same as in the previous section.

The middle and bottom right panels in Figure 5 demonstrate the robustness of the method we propose in this paper with respect to ΔDM . Figure 5 (middle right) shows the comparison between the recovered (from the noisy data) and the known structure parameters (from the noise-free intensity envelope that was time-shifted as per the group delay at each frequency). It shows that the filter recovers the correct structure parameters (to within a few percent) for all trial ΔDM s. To derive error bounds for ΔDM , we subtract the left-hand side of Equation (11) from the right-hand side of the same equation. This is shown in the bottom right panel of Figure 5. The uncertainty in ΔDM corresponds to those regions where the relative noise plus the intrinsic structure exceeds that of the structure at $\Delta DM = 0$, i.e., which can not be excluded by Equation (11). Thus, we find the error bounds by identifying the zero crossings in the bottom right panel, which suggest $\Delta DM = 0_{-0.04}^{+0.08} \text{ pc cm}^{-3}$.

4. Result: Application to FRB Data

The above methods can be applied to determine the correct DM of an FRB, and the uncertainty thereon. Dedispersing an FRB for many trial DMs produces a voltage time series that can

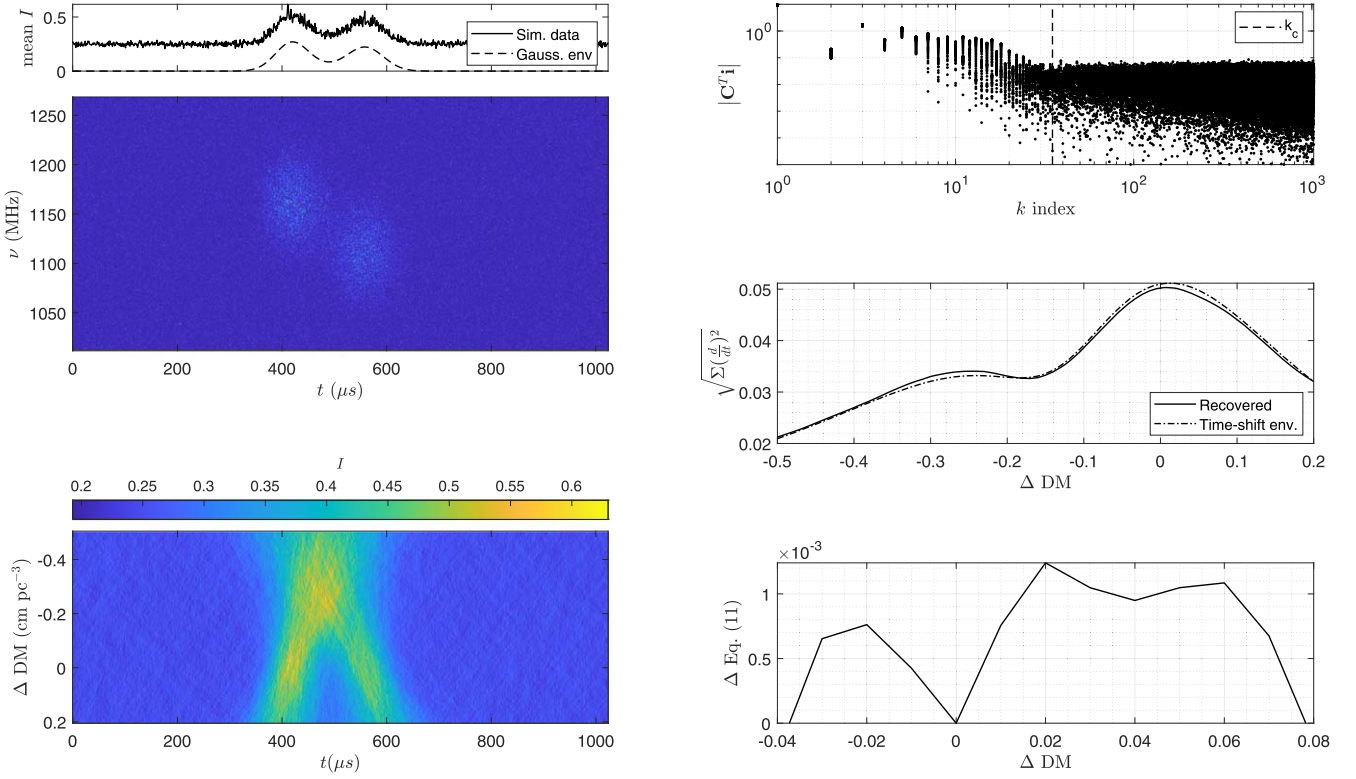


Figure 5. The top left and middle left panels show the simulated frequency down-drifting data at $\Delta\text{DM} = 0$. The top left panel shows the mean intensity over frequency of the noisy data (solid line) and the Gaussian envelope (dashed line) vs. time. The middle left panel is the frequency-time representation (dynamic spectrum) of the simulated data. The bottom left panel shows intensities vs. time and ΔDM of simulated frequency down-drifting data before filtering. The top right panel shows the DCT spectrum of the simulated noisy signal. The middle right panel reports the structure parameters of the recovered signal and the known structure parameter computed by applying time shifting based on the group delay to the envelope of the known signal. The bottom right panel shows the difference between the right- and left-hand sides of Equation (11); the error bounds are inferred from the zero crossings.

be converted into an intensity time series i . The procedure of Section 2 then produces a corresponding measure of the FRB structure and its uncertainty for each and every trial DM. This then allows the trial DM that maximizes structure to be identified, and also an error in DM that is assigned to include the range of trial DMs with a structure consistent with the maximum value, given the calculated structure error.

4.1. FRB 20181112A

We apply our method to FRB 20181112A (Cho et al. 2020) data averaged to $1 \mu\text{s}$. The middle left panel of Figure 6 shows the dynamic spectrum at $\Delta\text{DM} = 0$ and the bottom left panel shows the raw intensity data as a function of dispersion measure, away from the nominal value of $589.265 \text{ pc cm}^{-3}$ that produces the maximum S/N. The dedispersion about the nominal value is performed with the reference frequency set to the center of the bandwidth, in order to keep the temporal position of the pulse profile stable between different DM values. The spectrum of the intensity time series was obtained by the multiplication with the discrete cosine matrix discussed in Section 2.2. This is shown in the top right panel of Figure 6. We observe that the information occupies up to the $k = 35$ index, after which it is dominated by noise. Based on this information, we selected the filter cutoff of $k_c = 35$ and chose an $O = 3$ filter as per Equation (16).

The structure parameter and the corresponding uncertainty are plotted in the middle right and bottom right panels of Figure 6. We see that the highest structure coincides with $\Delta\text{DM} = 0$, which is the maximum S/N. The error bounds are

again identified by the zero crossings in the bottom right panel, which suggest $\Delta\text{DM} = 0_{-0.006}^{+0.009} \text{ pc cm}^{-3}$.

4.2. FRB 20210117A

Next, we consider FRB 20210117A (Bhandari et al. 2023) with time-domain data shown in Figure 7. The ΔDM , shown in the bottom left panel, is relative to the nominal S/N maximizing value of $729.21 \text{ pc cm}^{-3}$. This FRB appears to have a secondary peak for $\Delta\text{DM} < 0$. The spectrum of this FRB suggests a spectral transition at a k value between 20 and 30. We selected $k_c = 23$ and the $O = 3$ filter, which resulted in the structure parameter and the associated uncertainty plotted in the middle and bottom right panels in Figure 7. Using the same procedure as for FRB 20181112, we find a structure-maximizing $\Delta\text{DM} = -0.11_{-0.27}^{+0.25} \text{ pc cm}^{-3}$. Thus, we cannot exclude that this FRB's apparent structure-maximizing DM is significantly different from its signal-to-noise maximizing DM.

Figure 8 shows the best-fitting ΔDM and 68% uncertainty bounds as per Equation (11) over filter cutoff k_c (with $O = 3$). It confirms that $k_c \approx 25$ offers consistent values of the structure-maximizing ΔDM with the narrowest error margin. Using lower values of k_c results in oversmoothing, and thus a loss of signal structure, while using higher values of k_c adds noise, increasing the random error in ΔDM .

4.3. Implementation in CRAFT FRB Processing Pipeline

The structure-optimizing FRB method has been implemented for FRBs detected by the Australian Square Kilometre

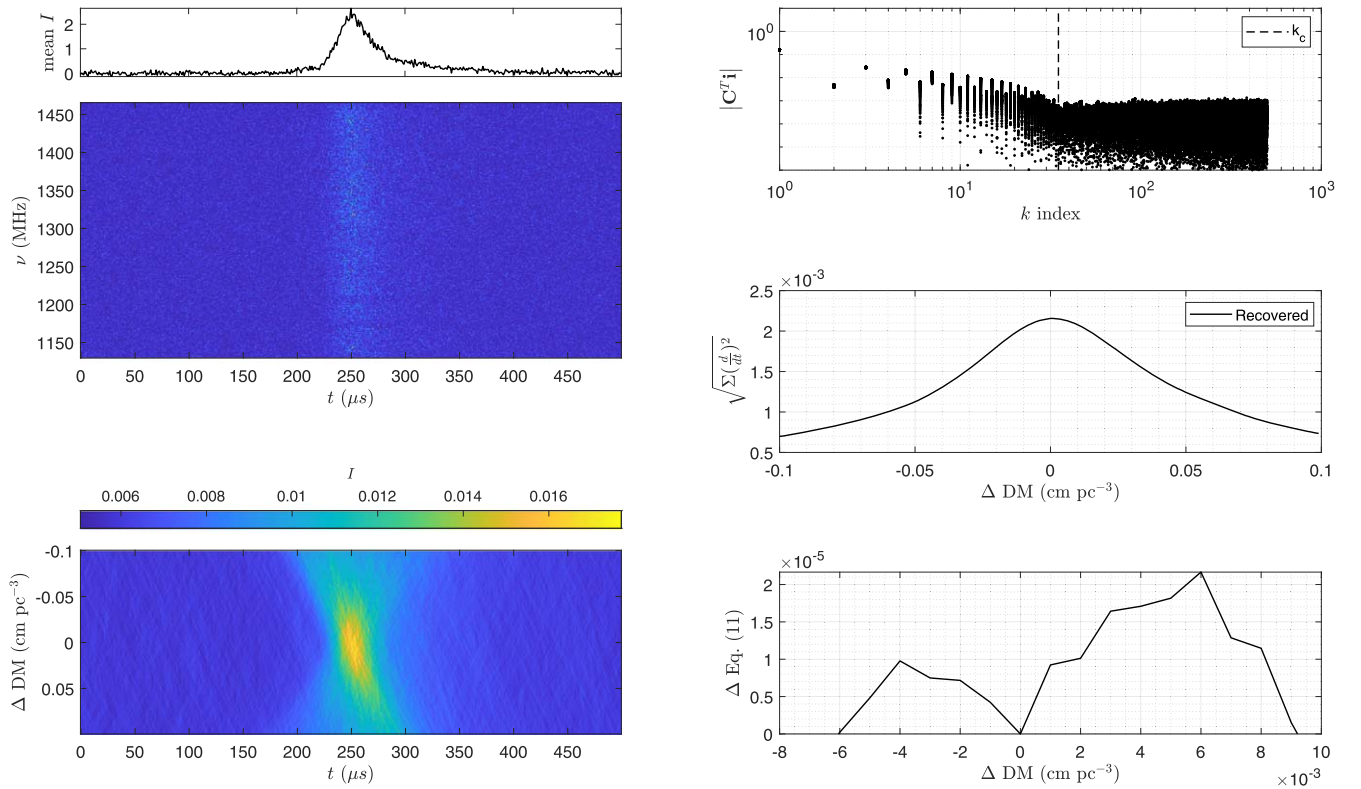


Figure 6. The top left panel shows the mean intensity over frequency of FRB 20181112A at Δ DM = 0 vs. time. The middle left panel is the dynamic spectrum of FRB 20181112A at Δ DM = 0 at 1μ s resolution. The bottom left panel shows intensities vs. time and Δ DM of FRB 20181112A at 1μ s resolution data before filtering. The top right panel shows the DCT spectrum of FRB 20181112A. The middle right panel reports the structure parameters of the recovered signal. The bottom right panel shows the difference between the right- and left-hand sides of Equation (11); the error bounds are inferred from the zero crossings.

Array Pathfinder (ASKAP; Hotan et al. 2021), as part of the Commensal Real-time ASKAP Fast Transients Survey (CRAFT; Bannister 2017) data processing pipeline, which runs on the OzStar supercomputer at the Centre for Astrophysics and Supercomputing at Swinburne University of Technology. Upon detecting an FRB candidate, raw voltages are read out from ASKAP buffers, transferred to OzStar, and processed by CELEBI, the CRAFT Effortless Localisation and Enhanced Burst Inspection Pipeline (Scott et al. 2023). This pipeline identifies the FRB in images and performs coherent beamforming, polyphase filterbank inversion, and coherent dedispersion to produce X and Y polarization complex voltages at $(336 \text{ MHz})^{-1} \approx 3 \text{ ns}$ resolution.

The DM structure-optimizing method extracts a $\pm 5 \text{ ms}$ window about the center of the FRB, which is automatically identified by CELEBI within the 3.1 s of voltage data. It then redisperses the data over a range of Δ DM about the nominal DM identified by the real-time detection pipeline, according to Equation (20). Typically, this range is $\pm 2 \text{ pc cm}^{-3}$ in intervals of 0.01 pc cm^{-3} . For each redispersion trial, the time series $i = |X|^2 + |Y|^2$ is calculated, integrated to a resolution of 1μ s, and operated on according to Section 2, using an $O = 3$ low-pass filter.

Both the maximized structure and its uncertainty are calculated for a range of k_c . A nominal value of k_c , k_{nom} , is first found as the smallest k with power below the noise level, which is estimated from the mean power in the upper 50% of k values. The range of k investigated is then $k_{\text{nom}} \pm 100$. The used value of k_c is that resulting in the smallest 68% confidence interval for Δ DM, represented by the smallest vertical distance between the dashed lines in Figure 8. Once the structure-

maximizing value has been identified, the relative uncertainty can be calculated according to Equation (9), allowing confidence intervals of Δ DM to be calculated according to Equation (11). This process takes approximately 15 min to run for each FRB. We note that the optimum values of k_c found this way (and the resulting structure-optimized DMs) are very close to, but not exactly the same as, the values of k_c chosen by eye.

5. Conclusion

We demonstrated that computing the structure parameter using the 2-norm, $\sqrt{\Sigma(d/dt)^2}$, permits a direct calculation of the uncertainty of the resulting structure parameter. The uncertainty of the first derivative of the smoothed data is calculated by taking the difference between the structure parameter of the smoothed data and the structure parameter of the “double-smoothed” data. The latter can be obtained easily by taking the smoothed data (before taking the derivative) and plugging it back as the input to the algorithm. We have also shown how to use this uncertainty for statistical tests for different intrinsic structures between two filtered signals.

This method was applied to FRB 20181112A and FRB 20210117A. In the case of FRB 20181112A, the DM that produces the highest S/N is the same as that with the highest structure within an uncertainty in Δ DM of $-0.006 \text{ pc cm}^{-3}$, $+0.009 \text{ pc cm}^{-3}$. As for FRB 20210117A, the highest structure occurred at a DM = $729.1_{-0.27}^{+0.25} \text{ pc cm}^{-3}$, compared to the signal-to-noise maximizing DM of 729.2 pc cm^{-3} .

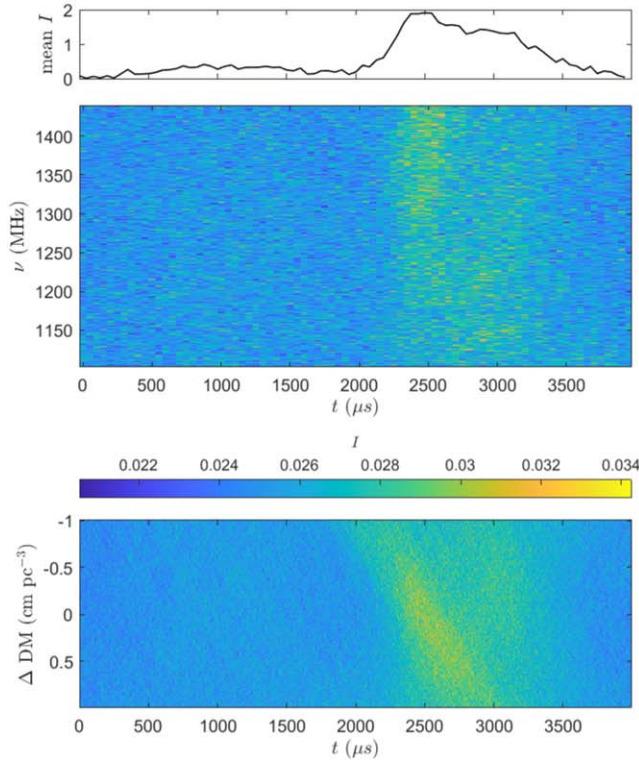


Figure 7. The top left panel shows the mean intensity over frequency of FRB 20210117A at $\Delta\text{DM} = 0$ vs. time. The middle left panel is the dynamic spectrum of FRB 20210117A at $\Delta\text{DM} = 0$ at $50 \mu\text{s}$ resolution. The bottom left panel shows intensities vs. time and ΔDM of FRB 20210117A data at $1 \mu\text{s}$ resolution before filtering. The top right panel shows the DCT spectrum of FRB 20210117A. The middle right panel reports the structure parameters of the recovered signal. The bottom right panel shows the difference between the right- and left-hand sides of Equation (11); the error bounds are inferred from the zero crossings.

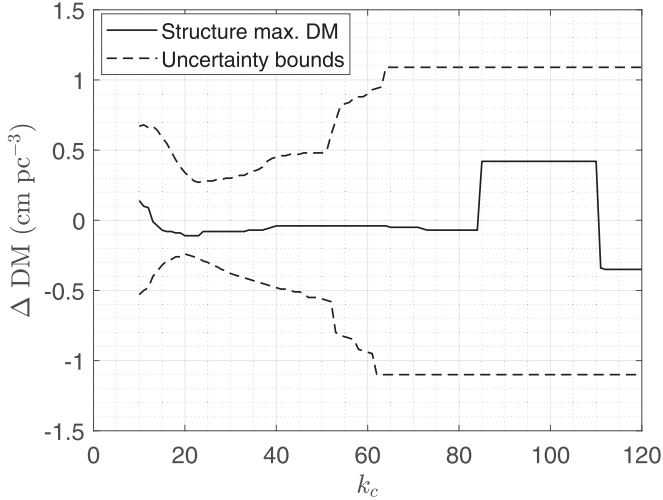
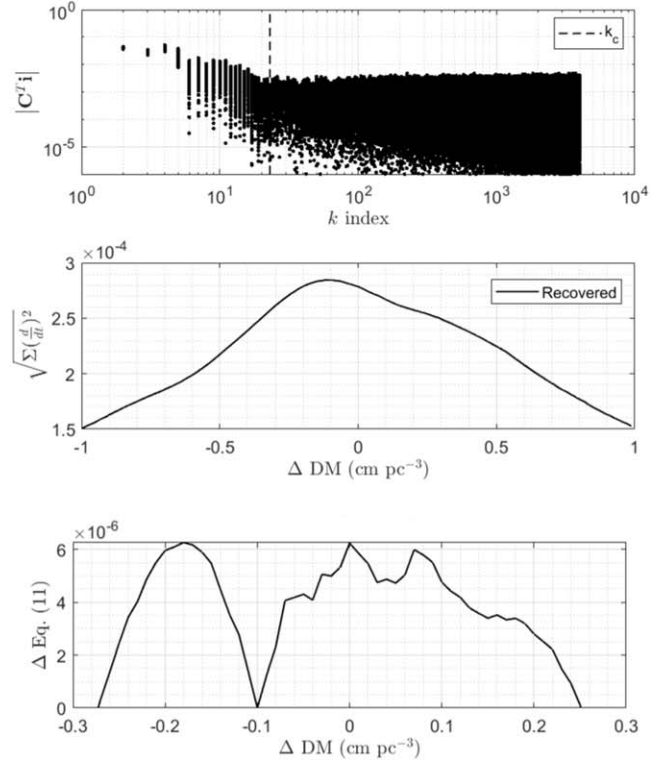


Figure 8. Structure-maximizing ΔDM (solid) and 68% error bounds (dashed) for FRB 20210117A as a function of filter cutoff k_c ($O = 3$).

Acknowledgments

The Australian SKA Pathfinder is part of the Australia Telescope National Facility (<https://ror.org/05qajvd42>), which is managed by CSIRO. Operation of ASKAP is funded by the Australian Government with support from the National Collaborative Research Infrastructure Strategy. ASKAP uses the resources of the Pawsey Supercomputing Centre. Establishment of ASKAP, the Murchison Radio-astronomy Observatory and the Pawsey Supercomputing Centre are initiatives of the Australian Government, with support from the Government of Western Australia and the



Science and Industry Endowment Fund. We acknowledge the Wajarri Yamatji people as the traditional owners of the Observatory site. This work was performed on the OzSTAR national facility at Swinburne University of Technology. The OzSTAR program receives funding in part from the Astronomy National Collaborative Research Infrastructure Strategy (NCRIS) allocation provided by the Australian Government, and from the Victorian Higher Education State Investment Fund (VHESIF) provided by the Victorian Government. C.W.J. and M.G. acknowledge support from the Australian Government through the Australian Research Council's Discovery Projects funding scheme (project DP210102103). This work made use of SCIPY (Virtanen et al. 2020).

Appendix

We now briefly discuss other definitions of structure parameters: $\Sigma(d/dt)^2$ (Hessels et al. 2019), $\Sigma|d/dt|$ (Gajjar et al. 2018), and $\Sigma(d/dt)^4$ (Joseph et al. 2019). We note that $\Sigma|d/dt|$ is the 1-norm of the vector derivative of the smoothed data (Strang 2019, see Ch.1). This means the triangle inequality is fulfilled, $\|\mathbf{x} + \mathbf{y}\|_1 \leq \|\mathbf{x}\|_1 + \|\mathbf{y}\|_1$ and the upper bound is defined. However, the inner product is not defined in the 1-norm (Strang 2019, see Ch.1). As a result, the corresponding lower bound cannot be shown to be that in Equation (8) for the 2-norm case.⁷ Furthermore, we are not able to relate the standard deviation estimate, such as Equation (6)










⁷ One can use the reverse triangle inequality to show $\|\mathbf{x} - \mathbf{y}\|_1 \geq \|\mathbf{x}\|_1 - \|\mathbf{y}\|_1$, but this is not the same as establishing the lower bound of $\|\mathbf{x} + \mathbf{y}\|_1$.

in the 2-norm, to a corresponding statistical quantity in the 1-norm.

$\Sigma(d/dt)^2$ and $\Sigma(d/dt)^4$ do not conform to the norm definition because they are missing \sim and \llcorner operators, which would have made them 2-norm and 4-norm, respectively (Laub 2005, see Ch. 7). Therefore, for these definitions, the triangle inequality does not apply and we are not able to establish the bounds of the summation of two vectors.

In Gajjar et al. (2018), the uncertainty of the structure parameter was inferred from the off-pulse system noise. This assumes that the noise during the FRB pulse is the same as that of the system noise. However, it is entirely possible that the FRB pulse is noise-like and hence the on-pulse noise is different from the off-pulse noise. In fact, the noise statistics of the FRB is in itself an interesting subject for study, and therefore, it is desirable that the uncertainty be inferred from that same on-pulse data.

ORCID iDs

Adrian T. Sutinjo  <https://orcid.org/0000-0002-9116-307X>
 Danica R. Scott  <https://orcid.org/0000-0002-6895-4156>
 Clancy W. James  <https://orcid.org/0000-0002-6437-6176>
 Marcin Glowacki  <https://orcid.org/0000-0002-5067-8894>
 Keith W. Bannister  <https://orcid.org/0000-0003-2149-0363>
 Hyerin Cho (조혜린)  <https://orcid.org/0000-0002-2858-9481>
 Cherie K. Day  <https://orcid.org/0000-0002-8101-3027>
 Adam T. Deller  <https://orcid.org/0000-0001-9434-3837>
 Ryan M. Shannon  <https://orcid.org/0000-0002-7285-6348>

References

- Bannister, K. W., Shannon, R. M., Macquart, J. P., et al. 2017, *ApJL*, **841**, L12
 Bhandari, S., Gordon, A. C., Scott, D. R., et al. 2023, *ApJ*, **948**, 67
 Caleb, M., Stappers, B. W., Abbott, T. D., et al. 2020, *MNRAS*, **496**, 4565
 CHIME/FRB Collaboration, Andersen, B. C., Bandura, K., Bhardwaj, M., et al. 2019, *ApJ*, **885**, L24
 Cho, H., Macquart, J.-P., Shannon, R. M., et al. 2020, *ApJL*, **891**, L38
 Eilers, P. H. C. 2003, *AnaCh*, **75**, 3631
 Gajjar, V., Siemion, A. P. V., Price, D. C., et al. 2018, *ApJ*, **863**, 2
 Hessels, J. W. T., Spitler, L. G., Seymour, A. D., et al. 2019, *ApJL*, **876**, L23
 Hilmarsson, G. H., Spitler, L. G., Main, R. A., & Li, D. Z. 2021, *MNRAS*, **508**, 5354
 Hotan, A. W., Bunton, J. D., Chippendale, A. P., et al. 2021, *PASA*, **38**, e009
 Josephy, A., Chawla, P., Fonseca, E., et al. 2019, *ApJ*, **882**, L18
 Laub, A. J. 2005, *Matrix Analysis for Scientists and Engineers* (Philadelphia, PA: SIAM)
 Lorimer, D. R., Bailes, M., McLaughlin, M. A., Narkevic, D. J., & Crawford, F. 2007, *Sci*, **318**, 777
 Macquart, J. P., Prochaska, J. X., McQuinn, M., et al. 2020, *Natur*, **581**, 391
 Michilli, D., Seymour, A., Hessels, J. W. T., et al. 2018, *Natur*, **553**, 182
 Pilia, M., Burgay, M., Possenti, A., et al. 2020, *ApJ*, **896**, L40
 Platts, E., Caleb, M., Stappers, B. W., et al. 2021, *MNRAS*, **505**, 3041
 Scott, D. R., Cho, H., Day, C. K., et al. 2023, *A&C*, **44**, 100724
 Stickel, J. J. 2010, *Comput. Chem. Eng.*, **34**, 467
 Strang, G. 1999, *SIAMR*, **41**, 135
 Strang, G. 2019, *Linear Algebra and Learning from Data* (Wellesley, MA: Wellesley-Cambridge Press)
 Strang, G., & Nguyen, T. Q. 1997, *Wavelets and Filter Banks* (Wellesley, MA: Wellesley-Cambridge Press)
 Virtanen, P., Gommers, R., Oliphant, T. E., et al. 2020, *NatMe*, **17**, 261
 Wilson, T. L., Rohlfs, K., & Hüttemeister, S. 2009, *Tools of Radio Astronomy* (Berlin: Springer), 19
 Zhao, Z. Y., Zhang, G. Q., Wang, Y. Y., Tu, Z.-L., & Wang, F. Y. 2021, *ApJ*, **907**, 111